SCIENCE CHINA
Chemistry

•ARTICLES•

September 2020 Vol.63 No.9: 1246–1255
https://doi.org/10.1007/s11426-020-9753-x

High-efficiency all-small-molecule organic solar cells based on an organic molecule donor with an asymmetric thieno[2,3-f]benzofuran unit

Rui Sun[1†], Yao Wu[1†], Jing Guo[1], Zhenghui Luo[2], Chuluo Yang[2] & Jie Min[1,3,4*]

[1]*The Institute for Advanced Studies, Wuhan University, Wuhan 430072, China;*
[2]*Hubei Key Lab on Organic and Polymeric Optoelectronic Materials, Department of Chemistry, Wuhan University, Wuhan 430072, China;*
[3]*Beijing National Laboratory for Molecular Sciences, Beijing 100190, China;*
[4]*Key Laboratory of Materials Processing and Mold (Zhengzhou University), Ministry of Education, Zhengzhou 450002, China*

Received March 17, 2020; accepted April 20, 2020; published online May 19, 2020

Two p-type small molecules BDTT-TR and TBFT-TR with benzo[1,2-b′:4,5-b′]dithiophene (BDT) and thieno[2,3-f]benzofuran (TBF) as central core units are synthesized and used as donors in all-small-molecule organic solar cells (all-SMOSCs) with a narrow-bandgap small molecule Y6 (2,2′-((2Z,2′Z)-((12,13-bis(2-ethylhexyl)-3,9-diundecyl-12,13-dihydro-[1,2,5]thiadiazolo[3,4-e]thieno[2″,3′′:4’,5′]thieno[2′,3′: 4,5]pyrrolo[3,2-g]thieno[2′,3′:4,5]thieno[3,2-b]indole-2,10-diyl)bis(methanylylidene))bis (5,6-difluoro-3-*oxo*-2,3-dihydro-1*H*-indene-2,1-diylidene))dimalononitrile) as the acceptor. In comparison to BDTT-TR with centrosymmetric BDT as the central unit, TBFT-TR with asymmetric TBF as the central unit shows red-shifted absorption, higher charge-carrier mobility and better charge pathway in blend films. The power conversion efficiency (PCE) of the all-SMOSCs based on TBFT-TR:Y6 reaches 14.03% with a higher short-circuit current density of 24.59 mA cm^{-2} and a higher fill factor of 72.78% compared to the BDTT-TR:Y6 system. The PCE of 14.03% is among the top efficiencies of all-SMOSCs reported in the literature to date.

thieno[2,3-f]benzofuran unit, small molecule donor, all-small-molecule system, absorption coefficient, crystallinity

Citation: Sun R, Wu Y, Guo J, Luo Z, Yang C, Min J. High-efficiency all-small-molecule organic solar cells based on an organic molecule donor with an asymmetric thieno[2,3-f]benzofuran unit. *Sci China Chem*, 2020, 63: 1246–1255, https://doi.org/10.1007/s11426-020-9753-x

1 Introduction

Solution-processed bulk-heterojunction (BHJ) organic solar cells (OSCs) have attracted substantial attention in recent years due to their unique advantages of low-cost, easy preparation, light-weight, and capability to be fabricated into large-scale colorful and flexible devices [1]. It is well known that the BHJ active layer of OSCs is composed of a n-type organic semiconductor (including fullerene derivatives, n-type conjugated polymer and n-type conjugated organic small molecule) as an acceptor and a p-type organic conjugated polymer or organic small molecule as a donor [1–13]. With continuous efforts on the materials design, morphology control and device engineering, the power conversion efficiencies (PCEs) have exceeded 16% for polymer donors [9–11,14–16] and over 13% for small molecule donors based OSCs [2,17,18], respectively, which is quite promising large-scale industrialization in the near future [1].

At present, most of the p-type conjugated polymer-based OSCs showed higher device performance in comparison with their organic small molecule-based counterpart, but polymer materials intrinsically suffer from variable average

†These authors contributed equally to this work.
*Corresponding author (email: min.jie@whu.edu.cn)

molecular weight (M_n) and polydispersity index (PDI) in different batch, hampering their commercial applications [3,19–21]. In contrast, small molecule donors which are easier to purify have well-defined structures, and thus have higher reproducibility and less batch-to-batch variation of their photovoltaic performance [22–26]. In consideration of the advantages of the organic small molecule materials and the lack materials diversity, attempts have been to develop all-small-molecule OSCs (all-SMOSCs) [2–8]. More recently, promising PCEs of over 13% were achieved in all-SMOSCs. The encouraging results exhibit that proper chemical structures of molecule materials and/or morphology control and device engineering can well address the corresponding issues associated with the low device performance in the all-SMOSCs such as mismatched visible-near infrared absorption spectra, low and/or unbalanced hole/electron transportation, and insufficient or excessive phase separation of the BHJ active layers [27–31]. The above-mentioned issues are very important to further improve photovoltaic performance of the all-SMOSCs [32–34].

For many reported all-SMOSCs, the highest occupied molecular orbit (HOMO) energy level of small molecule donor is deeper enough to exhibit higher open-circuit voltage (V_{oc}) in photovoltaic devices compared to their polymer's counterpart [2–8]. The main reason for poorer efficiency of the all-SMOSCs is mainly attributed to the lower short-circuit current density (J_{sc}) and fill factor (FF) values in the corresponding devices, limited by the charge carrier mobility and blend microstructures in the active layer. In general, a planar conjugated structure as an effective method can modify the molecular crystallinity and molecular ordering in the solid state. However, in the all-SM photovoltaic systems, the planar structures of donor and acceptor materials generally tend to be excessive mixture and hence form amorphous BHJ microstructures. It inevitably results in significant reductions in values of J_{sc} and FF, partly due to the dramatic gain in interfacial area and the poor or unbalanced charge transport properties. Thus, designing and selecting a matching photovoltaic system with high donor and acceptor molecular crystallinity, suitable phase separation and balanced domain sizes (to maximize J_{sc} and FF) is still a vital challenge for the all-small molecule photovoltaic systems.

In recent years, much important progress of PCEs achieved in the SMOSCs was associated with the BDT central core-based small molecule donors, and these molecules have become one of the major families of molecular photovoltaic materials [27–31]. For instance, several BDT-based molecules, including BSFTR [24], DCAO3TBDTT [25] and BTR-Cl [10], have been demonstrated to achieve PCE over 13% in the all-SMOSCs. Within the OSC community, BDT analogue, namely thieno [2,3-f]benzofuran (TBF), in which the thiophene ring of BDT unit is replaced with a furan ring, has been demonstrated [35,36]. Notably, as reported in the previous literatures involving polymer donor materials, compared with the BDT unit, the TBF unit possesses some unique features and advantages [35–37]. Compared with sulphur atom, the oxygen atom is less electron-rich which helps to tune the HOMO level and also provides stronger molecular aggregation [37]. In addition, in comparison with BDT-based compounds, excellent solubility and subtle change in aggregation behaviors can be expected in TBF derivatives due to inherent asymmetry [35,36]. Importantly, TBF derivatives possess a more planar structure, which can also modulate their blend microstructure in a controllable way [35–38]. Despite, the use of TBF unit in all-SMOSCs has not yet been investigated.

Herein we investigated the synergistic effect of the TBF central unit in small molecule donor materials for the all-SMOSCs. We designed and synthesized two small molecule donors, (5Z,5′Z)-5,5′-(((4,8-bis(5-(2-ethylhexyl)thio- phen-2-yl)benzo[1,2-b:4,5-b′]dithiophene-2,6-diyl)bis(3,3′′- dioctyl-[2,2′:5′,2′′-terthiophene]-5′′,5diyl))bis (methanylylidene))bis (3-ethyl-2-thioxothiazolidin-4-one) (BDTT-TR) and (5Z,5′Z)-5,5′-(((4,8-bis(5-(2-ethylhexyl)thiophen-2-yl) thieno[2,3-f]benzofuran-2,6-diyl)bis (3,3′′-dioctyl-[2,2′:5′,2′′-terthiophene]-5′′,5-diyl))bis(methanylylidene))bis(3-ethyl-2-thioxothiazolidin-4-one) (TBFT-TR), as shown in Scheme 1. Benefiting from the investigated material properties and critical devices processing, our in-depth study reveals the underlying structure-property relationships in these two photovoltaic systems. The PCE of the all-SMOSCs with TBFT-TR as the donor and Y6 (2,2′-((2Z,2′Z)-((12,13-bis(2-ethylhexyl)-3,9-diundecyl-12,13-dihydro-[1,2,5]thiadiazolo [3,4-e]thieno[2″,3′′:4’,5′]thieno[2′,3′:4,5]pyrrolo[3,2-g]thieno[2′,3′:4,5]thieno[3,2-b]indole-2,10-diyl)bis(methanylylidene))bis(5,6-difluoro-3-*oxo*-2,3-dihydro-1*H*-indene-2,1-diylidene))dimalononitrile) as the acceptor reached 14.03% with a high V_{oc} of 0.784 V, an enhanced J_{sc} of 24.59 mA cm^{-2} and a higher FF of 72.78%, compared to the BDTT-TR:Y6 photovoltaic system. The PCE of 14.03% is one of the highest values reported in literature to date for the all-SMOSCs. Notably, devices based on other fullerene and non-fullerene acceptors including $PC_{71}BM$ ([6,6]-phenyl-C71-butyric acid methyl ester), IDIC ((2,2′-((2Z,2′Z)-((4,4,9,9-tetrahexyl-4,9-dihydro-s-indaceno[1,2-b:5,6-b′]dithiophene-2,7-diyl)bis(methanylylidene))bis(3-*oxo*-2,3-dihydro-1*H*-indene-2,1-diylidene))dimalononitrile) and Y6-C2 ((2,2′-((2Z,2′Z)-((12,13-bis(3-ethylheptyl)-3,9-diundecyl-12,13-dihydro-[1,2,5]thiadiazolo[3,4-e]thieno[2″,3′′:4′,5′] thieno [2′,3′:4,5]pyrrolo[3,2-g]thieno[2′,3′:4,5]thieno[3,2-b]indole-2,10-diyl)bis(methaneylylidene))bis(5,6-difluoro-3-*oxo*-2,3-dihydro-1*H*-indene-2,1-diylidene)dimalononitrile) were also fabricated, highlighting that TBFT-TR is a universal and high-performance small molecule donor.

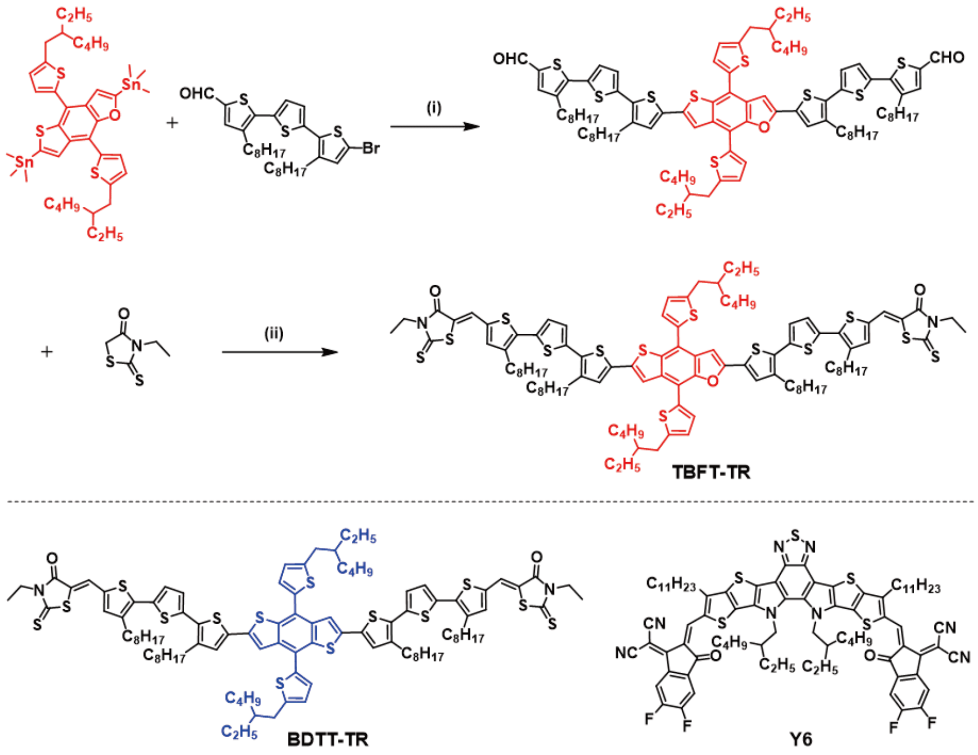

Scheme 1 Synthesis route of TBFT-TR and the chemical structures of the two small molecules (TBFT-TR and BDTT-TR) and Y6 acceptor. Reaction conditions: (i) $Pd(PPh_3)_4$, toluene, 110 °C, 24 h, yield 60%; (ii) piperidine, $CHCl_3$, 74 °C, overnight, yield 89% (color online).

2 Results and discussion

2.1 Materials synthesis and characterization

The synthetic route of the small molecule donor TBFT-TR is depicted in Scheme 1. The target small molecules BDTT-TR and TBFT-TR were synthesized through two-step reactions of Still-coupling followed by Knoevenagel condensation (Figures S1–S5, Supporting Information online). The monomers and donors were synthesized according to the procedures shown in our previous publications [39,40]. Scheme 1 also shows the molecular structures of the synthesized BDTT-TR donor and the reported Y6 acceptor [41]. Both of the two small molecule donors possess good solubility in common organic solvents such as chloroform and chlorobenzene.

Density functional theory (DFT) was performed to calculate the optimal geometries of BDTT-TR and TBFT-TR, as shown in Figure 1(a). Compared to the torsional angle of BDT-Th unit (13.37°), TBF-Th unit shows a lower torsional angle of 2.93°. It might be ascribed to smaller size of oxygen atom which lowers the steric hindrance between TBF and thiophene unit. This indicates that TBFT-TR has a better planarity. The dipole moments of TBF and BDT were also calculated to gain deep insights into the distinctions between asymmetrical and symmetrical core of the two small molecule donors. BDT is centrosymmetric with dipole moment of nearly 0, while TBF unit has dipole moment of 1.21 Debye. When chromophores possess large dipole-moment, strong intermolecular dipole-dipole interactions can be expected which drives neighboring molecules to align antiparallel to each other, resulting in higher order in solid films [42–45]. The DFT-calculated HOMO/lowest unoccupied molecular orbit (LUMO) energy levels of BDTT-TR and TBFT-TR are −4.92/−2.79 and −4.90/−2.79 eV, respectively, as exhibited in Figure S6. In addition, the HOMO energy levels were also measured by cyclic voltammetry (Figure S7(a)). The calculated $E_{HOMO/LUMO}$ for BDTT-TR and TBFT-TR are −5.17/−3.43 eV and −5.16/−3.46 eV (Figure S7(b)), which is consistent with the DFT calculation.

Normalized absorption spectra of BDTT-TR and TBFT-TR molecule donors in the thin films, as well as the reference spectra of Y6 acceptor in the thin film are exhibited in Figure 1(b) and the corresponding optical data are summarized in Table S1 (Supporting Information online). The UV-Vis absorption spectra of these two molecules in films show an obvious red-shifted and broadened absorption. As compared to the absorption spectra of BDTT-TR, TBFT-TR is slightly more red-shift by 19 nm at the optical absorption edge (E_g^{opt}) corresponding to a bandgap of 1.71 eV. In addition, the higher and broader absorption shoulder of TBFT-TR around 640 nm suggests that the intermolecular packing of TBFT-TR is better than that of BDTT-TR in the solid state. Notably, the oscillator strength (f_1) values are calculated for these two molecules in the linear all-*cis* configuration [46]. TBFT-TR

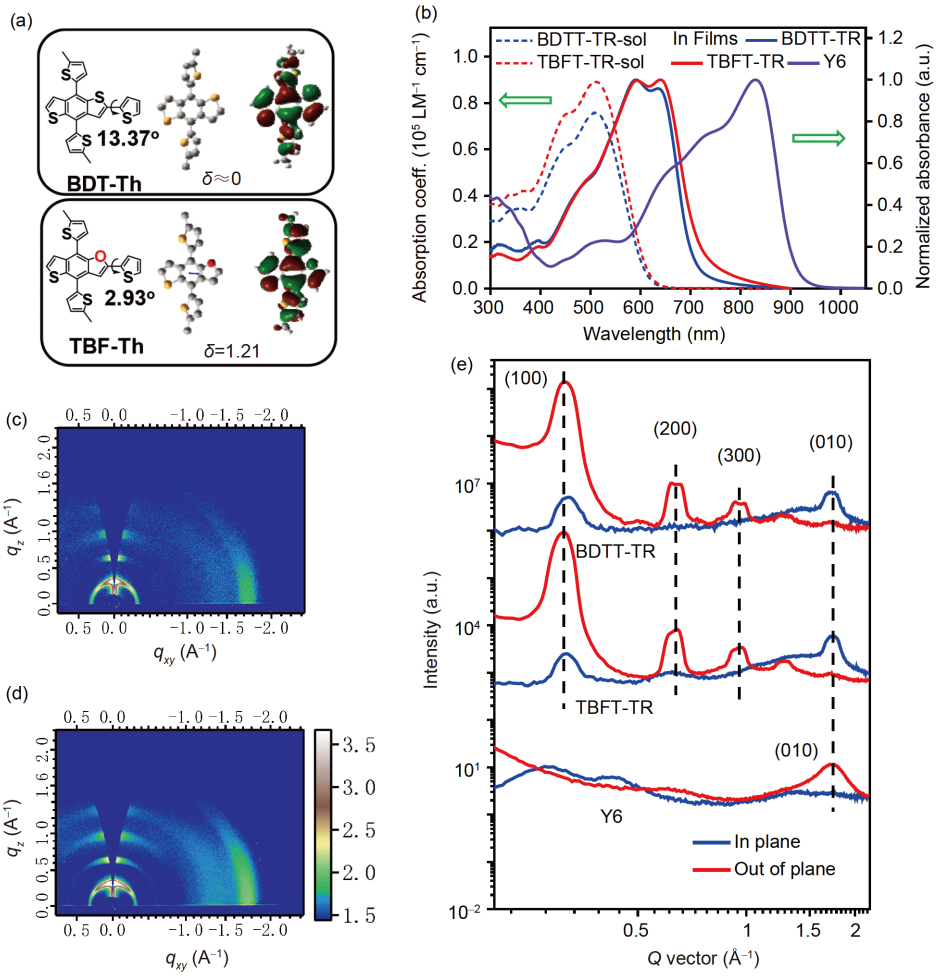

Figure 1 (a) The twisting effects of BDT-Th and TBF-Th, the dipole moments and HOMO surface of BDT and TBF. (b) Optical properties of BDTT-TR, TBFT-TR and Y6. (c, d) GIWAXS images of neat BDTT-TR, and TBFT-TR. (e) GIWAXS intensity profiles along the OOP (red line) and IP (blue line) directions acquired at the critical incident angle of 0.13° (color online).

exhibits a higher value of f_1 (2.94) than that of BDTT-TR (2.03). The result is also in good agreement with the measured absorption coefficients of 0.75×10^5 M^{-1} cm^{-1} for BDTT-TR and 0.89×10^5 M^{-1} cm^{-1} for TBFT-TR in solutions, respectively, as presented in Figure 1(b). The higher f_1 of TBFT-TR molecule is able to absorb more photons in the blend film, which can be favorable for better charge generation [46].

The grazing incidence wide-angle X-ray scattering (GIWAXS) measurements were employed to investigate the molecular packing information of the neat films. Figure 1(c, d) show the two-dimensional (2D) diffraction images of the neat films for BDTT-TR and TBFT-TR, respectively. The corresponding intensity profiles in the out-of-plane (OOP) and in-plane (IP) directions are presented in Figure 1(e). Both show the obvious vector q of 1.73 $Å^{-1}$ on the q_{xy} axis, which attributes the π-π diffraction peak (010) in the IP direction. It can be also found that the obvious scattering vector q of 0.3, 0.6, and 0.9 $Å^{-1}$ on the q_z axis originates from lamellar packing diffraction (100, 200, and 300) in the OOP direction, implying a high degree of molecular ordering and a predominant edge-on molecular orientation. In addition, as compared to the BDTT-TR film with the π-π stacking at q_{xy}= 1.72 $Å^{-1}$ (d~3.65 Å), TBFT-TR shows slightly more compact π-π stacking diffraction (010) with the vector q of 1.74 $Å^{-1}$ on the q_{xy} axis, corresponding to a π-π stacking distance of 3.61 $Å^{-1}$. The stronger π-π stacking signals and the smaller π-π stacking distance of TBFT-TR can be ascribed to its better planarity, which is beneficial to accelerate the hole transport behavior. The hole mobility of BDTT-TR and TBFT-TR were therefore investigated by using the space charge limited current (SCLC) measurements (Figure S8 and Table S2). The hole mobility of TBFT-TR is 3.33×10^{-4} cm^2 V^{-1} s^{-1}, which is approximately two times higher than that of BDTT-TR (1.39×10^{-4} cm^2 V^{-1} s^{-1}), reflecting the morphology results from above. The higher carrier mobility of TBFT-TR indicates that the oxygen-substitution is beneficial to molecular ordering in the thin film yielding better intramolecular electron transport. Besides, as shown in Figure S9, the neat Y6 film shows a strong π-π stacking peak in the

OOP direction at q=1.74 Å^{-1}, indicating a preferential face-on orientation of Y6, which is consistent with the other reported results [41].

2.2 Photovoltaic performance

To investigate the photovoltaic properties of these two small molecule donors BDTT-TR and TBFT-TR, we fabricated the all-SMOSCs with a conventional architecture of indium tin oxide (ITO)/poly(3,4-ethylenedioxythiophene):poly(styrenesulfonate) (PEDOT:PSS)/active layer (BDTT-TR or TBFT-TR blend with Y6)/perylene diimide functionalized with amino *N*-oxide (PDINO)/Al. The device performance was optimized by varying the weight ratio of the donor/acceptor (Figure S10), the conditions of thermal annealing (TA) treatments (Figures S11 and S12), the solvent vapor annealing (SVA) treatments (Figure S13) and coating speeds (Figure S14), respectively. The detailed optimization parameters are summarized in Tables S3–S7. The optimal photovoltaic performances of the as-cast and TA based devices are shown in Table 1, and the current-density-voltage (*J*-*V*) characteristics of the corresponding devices are exhibited in Figure 2(a). For the as-cast devices, significantly low PCEs of 0.12% for BDTT-TR:Y6 blend and 0.19% for TBFT-TR:Y6 active layers were obtained. In this work, TA treatment is a key factor for improving the device performance of these two photovoltaic systems. Both blends exhibited the best photovoltaic performances with a D:A weight ratio of 1.8:1, followed by TA treatments at 140 °C for 2 min. The optimal BDTT-TR:Y6 blend exhibited the best PCE of 12.18%, with a V_{oc} of 0.780 V, a J_{sc} of 23.64 mA cm^{-2}, and a FF of 66.06%. Meanwhile, the optimized TBFT-TR:Y6 device shows significantly higher J_{sc} (24.59 mA cm^{-2}) and FF (72.78%) values compared to the BDTT-TR:Y6 devices, and thus results in an increased PCE of 14.03%. The statistical photovoltaic metrics and PCE histogram were obtained from 30 individual devices as presented in Figure 2(b), which indicate the good reproducibility of photovoltaic performance of the BDTT-TR:Y6 and TBFT-TR:Y6 devices.

The main contribution to the PCE enhancement in the TBFT-TR:Y6 device is from the J_{sc} and FF improvements. The external quantum efficiency (EQE) curves provided in Figure 2(c) can effectively confirm the above-mentioned J_{sc} improvements. The calculated current densities (J_{EQE}) were 23.29 and 24.09 mA cm^{-2} for TA-based BDTT-TR:Y6 and TBFT-TR:Y6 devices, respectively, which matched well with the J_{sc} values obtained from *J*-*V* curves measured under one sun illumination. It should be noted that the TBFT-TR-based devices show higher photo response than the BDTT-TR:Y6 devices, especially in the wavelength range from 360 to 720 nm. Such EQE enhancement is also in good agreement with the stronger photo absorption of the TA-based TBFT-TR:Y6 blend than that of the corresponding BDTT-TR:Y6 blend (Figure S15), possibly resulting from the higher oscillator strength and absorption coefficient of TBFT-TR molecules. Of note is that the improvement in device performance of TBFT-TR:Y6 system, especially for FF, was attributed to combined effects of a number of factors, which will be discussed in below.

In order to further highlight the advantages of small molecule donor TBFT-TR, we applied these two small molecules to fabricate with other efficient fullerene and non-fullerene acceptors, including $PC_{71}BM$, IDIC, and Y6-C2 [47]. The *J*-*V* curves of these optimized devices are shown in Figure 2(d) and Figures S16–S18, and the corresponding photovoltaic parameters are also summarized in Table 1. Similar to the Y6-based systems, all the devices based on TBFT-TR as donor blending with $PC_{71}BM$, IDIC, or Y6-C2 as acceptor exhibited the higher J_{sc} and FF values and thus achieved the better PCE values as compared to the BDTT-TR-based photovoltaic systems. These results indicate that TBFT-TR is a universal and effective molecule donor for the OSCs.

Table 1 Summary of photovoltaic parameters for the BDTT-TR- and TBFT-TR-based photovoltaic systems

Active layers	Conditions	V_{oc} (V)	J_{sc} (mA cm^{-2})	J_{EQE} [a)] (mA cm^{-2})	FF (%)	PCE (%, PCE[b)])
BDTT-TR:Y6	As-cast	0.868	0.61	0.59	22.25	0.12 (0.10)
BDTT-TR:Y6	TA	0.780	23.64	23.29	66.06	12.18 (12.02)
TBFT-TR:Y6	As-cast	0.879	0.95	0.95	22.18	0.19 (0.14)
TBFT-TR:Y6	TA	0.784	24.59	24.09	72.78	14.03 (13.84)
BDTT-TR:$PC_{71}BM$	As-cast	0.917	13.41	12.62	70.78	8.71 (8.42)
TBFT-TR:$PC_{71}BM$	As-cast	0.903	13.80	13.20	76.10	9.48 (9.28)
BDTT-TR:IDIC	SVA	0.882	12.09	11.56	67.75	7.22 (7.00)
TBFT-TR:IDIC	SVA	0.882	12.52	12.04	72.06	7.96 (7.80)
BDTT-TR:Y6-C2	TA	0.765	23.10	22.79	67.75	11.92 (11.68)
TBFT-TR:Y6-C2	TA	0.774	24.50	23.35	72.57	13.76 (13.50)

a) J_{EQE} represents the integrated current density obtained from EQE spectra. b) The average values for ten devices in the brackets.

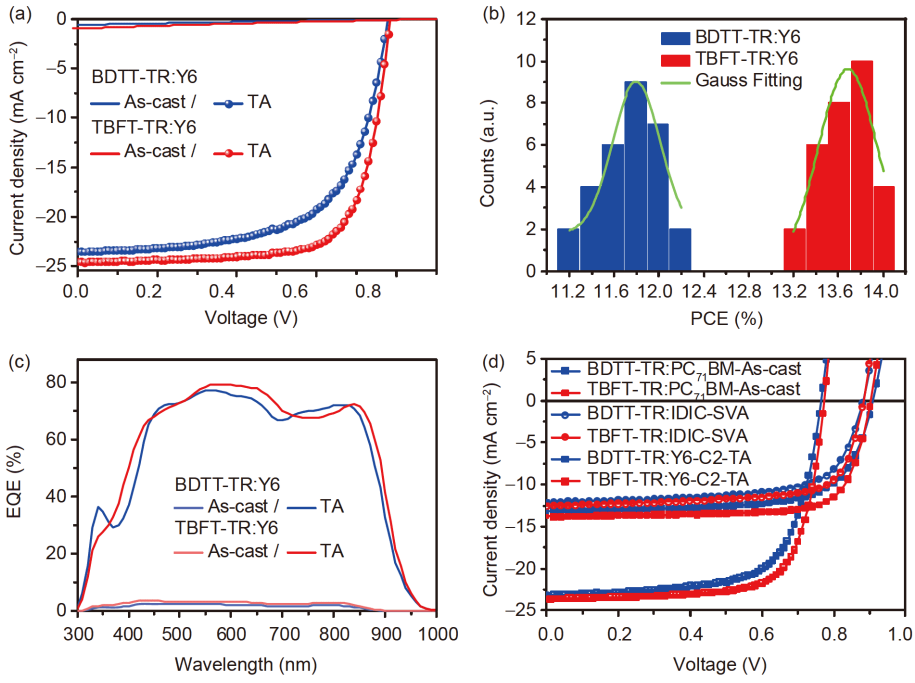

Figure 2 (a) The *J-V* curves of the as-cast and TA-based BDTT-TR:Y6 and TBFT-TR:Y6 solar cells. (b) Histogram of PCE counts for 30 individual devices with the BDTT-TR:Y6 active layer and TBFT-TR:Y6 active layer, respectively. (c) The EQE curves of the best-performing devices. (d) The *J-V* curves of BDTT-TR:PC$_{71}$BM/IDIC/Y6-C2 and TBFT-TR:PC$_{71}$BM/IDIC/Y6-C2-based solar cells (color online).

2.3 Comparative analysis of device performance

As mentioned above, the photovoltaic performance of OSCs is sensitive to many aspects, such as the material properties, the molecular interactions and the physical mechanisms caused by the specific blend characteristics. By carefully reviewing these two photovoltaic systems, we can easily find that their performance differences (12.18% for BDTT-TR:Y6 and 14.03% for TBFT-TR:Y6) are mainly due to the differences in J_{sc} and FF values. In order to figure out the difference of photovoltaic performance, the exciton dissociation and charge collection characteristics were firstly evaluated by measuring the photocurrent density (J_{ph}), which is defined as $J_{ph}=J_L-J_D$ (where J_D and J_L are the current densities in the dark and under one sun illumination), and the effective voltage (V_{eff}) given by $V_{eff}=V_o-V$ (where V_o is the voltage at which J_{ph} is 0 and V is the applied voltage) [1]. When the $V_{eff}>>2.0V$, the saturated J_{ph} (J_{sat}) of the TBFT-TR:Y6 device is 25.97 mA cm^{-2}, which is slightly higher than that (J_{sat}=25.60 mA cm^{-2}) of the BDTT-TR:Y6 device (Figure 3(a)). The photoluminescence (PL) spectroscopy finds quenching efficiencies of 94.1% for BDTT-TR:Y6 blend and 97.7% for TBFT-TR:Y6 blend, respectively, as presented in Figure S19. The results reflect that most of excitons can be effectively separated into free charges in these two optimized blends. In addition, the exciton dissociation probability (P_{diss}) under the short-circuit conditions can be confirmed by measuring the J_{ph}/J_{sat}. The P_{diss} values of BDTT-TR:Y6 and TBFT-TR:Y6 devices were calculated to be 97.20% and 98.06%, respectively, demonstrating that both systems also possess efficient charge collection efficiency. Nevertheless, we found that the extraction time of the optimized BDTT-TR:Y6 device was extracted to be τ=0.60 μs, evaluated by transient photocurrent (TPC) measurements (Figure 3(b)), which is longer than that (τ=0.29 μs) of the optimized TBFT-TR:Y6 device. This result indicates that the differences in J_{sc} and FF observed are associated to the rate of charge extraction in the corresponding devices, probably resulting from the different charge transport properties and non-geminate recombination rates.

To quantify the charge transport properties of the optimized blends, the SCLC were measured, as provided in Figures S20 and S21, respectively. The average hole mobilities (μ_h)/electron mobilities (μ_e) of BDTT-TR:Y6 and TBFT-TR:Y6 devices were calculated to be 1.39×10^{-4}/8.58×10^{-4} and 5.21×10^{-4}/8.99×10^{-4} cm^2 V^{-1} s^{-1} (Figure 3(c)), which corresponded to the μ_h/μ_e ratios of 0.27 and 0.58, respectively, as presented in Table S8. Obviously, the enhanced and well-balanced transport in the TBFT-TR:Y6 blend could effectively prevent the charge accumulation and recombination, contributing to larger FF in the resulting devices.

To get insights into the effects of TBF and BDT central units on the charge recombination behaviors in the devices, the corresponding J_{sc} and V_{oc} *versus* light intensity (P_{light}) were measured firstly. The relationship between the J_{sc} and

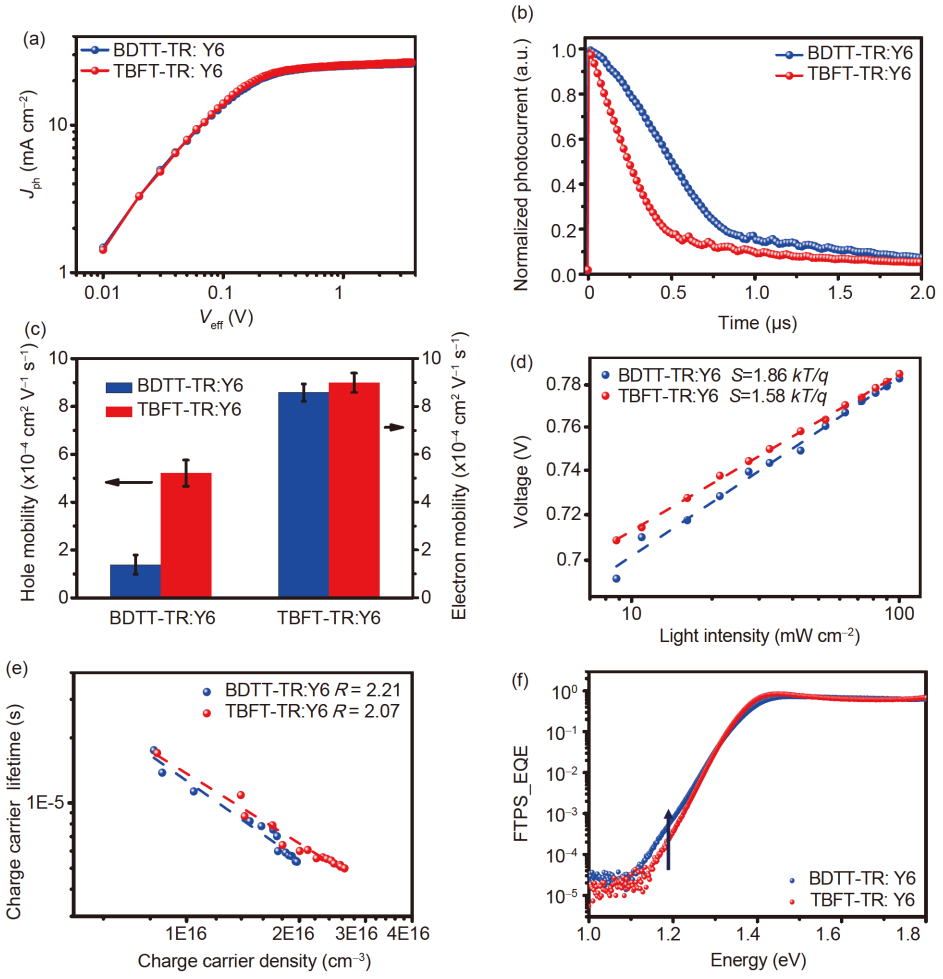

Figure 3 (a) The evolution of J_{ph} *versus* V_{eff} for the optimized devices. (b) Normalized TPC data for the optimized devices. (c) Hole-only and electron-only mobilities of the optimized devices. (d) The light intensity dependence of V_{oc} for the optimized devices. (e) The evolution of carrier lifetime *versus* carrier density under V_{oc} conditions. (f) Comparison of the normalized FTPS spectra of the optimized devices (color online).

P_{light} can be interpreted based on the formula, $J_{sc} \propto P_{light}^{s}$, in which the exponential factor s denotes the degree of bimolecular recombination [48]. The best fit for the data is obtained when the value s is close to unity, which indicates negligible bimolecular recombination during sweep-out. As shown in Figure S22, the s value of the BDTT-TR:Y6 device is 0.98, whereas that of TBFT-TR:Y6 device is 1.00, suggesting that a slightly stronger bimolecular recombination occurs in optimized BDTT-TR-based device. In contrast, such negligible bimolecular recombination facilitated higher J_{sc} and FF values for the optimized TBFT-TR-based device. Additionally, the light intensity dependence of V_{oc} data is fitted to the linear law: $V_{oc} \propto nkT/q \ln P_{light}$ (Figure 3(d)), where k, T, and q are the Boltzmann constant, the temperature in Kelvin, and the elementary charge, respectively. The slopes for BDTT-TR:Y6 and TBFT-TR:Y6 devices are 1.86 kT/q and 1.58 kT/q, respectively. The stronger dependence of V_{oc} on P_{light} implies that carrier dynamics at open circuit in the optimized BDTT-TR:Y6 device is more governed by a combination of trap-assisted (Schockley-Real-Hall) type and bimolecular recombination as compared with the TBFT-TR:Y6 device. This can be useful for explaining the higher J_{sc} value of the TBFT-TR:Y6 device due to the beneficial microstructural intermixing as described in below.

Here we also conducted the transient photovoltage (TPV) and charge extraction (CE) measurements, as shown in Figure 3(e). Normally, a non-geminate recombination order R (R=λ+1) can be calculated *via* the equation $\tau = \tau_0 (n_0/n)^{\lambda}$, where λ is the so-called recombination exponent, τ_0 (adopted from TPV curves, Figure S23) and n_0 (calculated from CE curves, Figure S24) are constants. The optimized BDTT-TR:Y6 device exhibits a higher recombination order value (R=2.21) than that (R=2.07) of the optimized TBFT-TR:Y6 device, indicating the more traps or defects in the optimized BDTT-TR:Y6 blends. This conclusion is further demonstrated by the Fourier-transform photocurrent spectroscopy (FTPS) measurements. As shown in Figure 3(f), the optimized BDTT-TR:Y6 device showed the larger density of

subgap states in the regime between 1.10 and 1.25 eV as compared to the TBFT-TR:Y6 device. This result is associated with the relevant physical characterizations as mentioned above. Overall, the results of the exciton dissociation properties and charge extraction properties coupled with the evaluation of charge carrier mobilities and the analysis of the carrier recombination dynamics give detailed insight into subtle mechanisms being responsible for the corresponding J_{sc} and FF values. Actually, these relationships between physical dynamic and device performance are mainly controlled by the morphology characterizations, which will be discussed in below.

2.4 Morphology analysis

Before discussing morphological characteristics, we firstly mention the influence of TA treatments on film properties *via* UV-Vis absorption spectroscopy (Figure S15). As compared to the as-cast blended films, both annealing films show red-shifted absorption spectra and distinct absorption peaks at approximately 600 nm, indicating simultaneously enhanced aggregation of donor and acceptor materials. Here we further employed atomic force microscopy (AFM), transmission electron microscopy (TEM) and GIWAXS to directly understand the observed changes in optical properties upon TA treatments, and the nature of the molecular order in these two optimized blends.

The tapping-mode AFM, TEM were utilized to investigate the phase separated morphology, as shown in Figures S25 and S26. AFM shows rather uniform surfaces for the as-cast- and TA-based films with small root-mean-square (RMS) surface roughness values. As compared to the as-cast films, the BDTT-TR:Y6 and TBFT-TR:Y6 annealed films showed more phase separation with obvious bi-continuous interpenetrating network characteristics. In addition, more insight into the bulk microstructure came from TEM investigations. The non-annealed films, especially for BDTT-TR:Y6 blend, exhibit almost no discernible structure, suggesting a strongly inter-mixed D:A microstructure without any significant crystallization or phase separation. These characteristics of blend morphologies based on the as-cast layers can be used strongly to explain their poor photovoltaic performance in devices (Figure 2(a)). In contrast, in the case of TA films the formation of separated D/A domains with a bi-continuous interpenetrating network becomes clearly discernible, especially for the TBFT-TR:Y6 blend (Figure S26(d)). The 2D GIWAXS patterns of the relevant as-cast and annealed films depicted in Figure 4 also demonstrated the results of the AFM and TEM images (Figures S25 and S26). The as-cast films feature only scattering rings with the π-π stacking peak area located at 1.70 and 1.72 $Å^{-1}$ for BDTT-TR:Y6 and TBFT-TR:Y6, respectively. In contrast, both annealed films display well defined molecular stacking with diffraction peaks. From these data we imply that mixing Y6 with BDTT-TR or TBFT-TR disturbs the molecular ordering of donor and acceptor molecules, which can be only recovered by annealing.

The crystallization behaviors of the optimized systems are further discussed by probing the well-defined IP (010) peak originating from BDTT-TR or TBFT-TR π-π stacking as shown in Figure 4(b, d), respectively. From the 1D GIWAXS profiles, as presented in Figure 4(e), the annealed BDTT-TR:Y6 blend exhibits relatively weak peak at 1.73 $Å^{-1}$ from BDTT-TR π-π stacking, and also possesses weak OOP (200 and 300) peaks. The results suggest that the BDTT-TR:Y6 blend is slightly less ordered as compared to the TBFT-TR:Y6 blends, even though both annealed blends show preferable face-on orientation of Y6 molecules. Furthermore, the

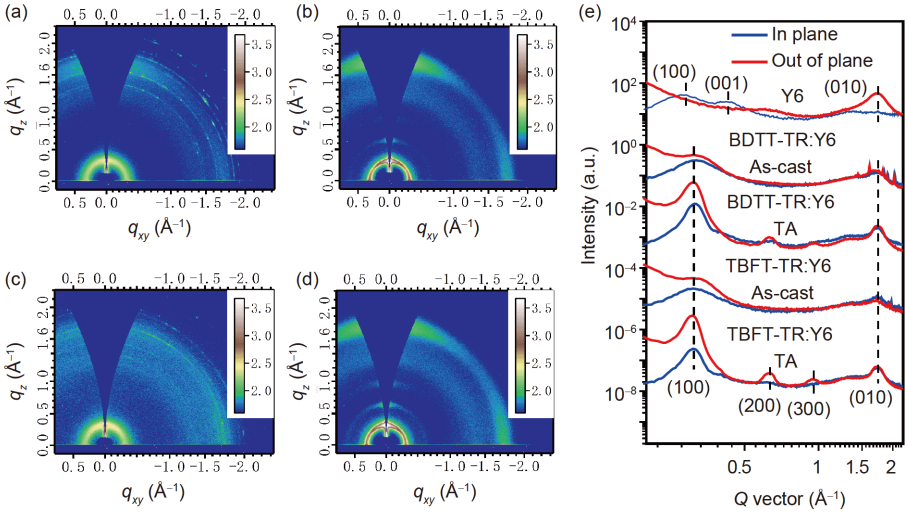

Figure 4 2D GIWAXS patterns of the TBFT-TR:Y6 and TBFT-TR:Y6 blend films without and with TA treatment: (a) BDTT-TR:Y6 as-cast, (b) BDTT-TR:Y6 TA, (c) TBFT-TR:Y6 as-cast and (d) TBFT-TR:Y6 TA, respectively. (e) The 1D GIWAXS line curves with respect to the IP and OOP directions. The IP and OOP profiles of the blend films acquired at the critical incident angle of 0.13° (color online).

Scherrer equation was employed to calculate the crystal coherence lengths (CCL) of the BDTT-TR and TBFT-TR crystallites [4]. The CCL (010) in the IP direction of the annealed TBFT-TR:Y6 blend is 36.51 Å, which is higher than that (30.94 Å) of the annealed BDTT-TR:Y6 blend (Table S9), also indicating BDTT-TR molecules induce lower molecular ordering than TBFT-TR molecules when blending with Y6. Overall, the choice of small molecules enables fine-tuning the molecular ordering in the BHJ blends. This, in turn, is likely to cause changes in the physical mechanisms and photovoltaic parameters in the corresponding devices. Notably, the suitable phase separation with better molecular ordering in the annealed TBFT-TR:Y6 blend leads to the better performance of the TBFT-TR-based OSCs.

3 Conclusions

In summary, the two 2D-conjugated small molecules BDTT-TR and TBFT-TR with different central units were developed and used as donors in the all-SMOSCs with low bandgap small molecule Y6 as acceptor. Compared to analogous BDT-cored small molecule BDTT-TR, TBFT-TR based on TBF as central core enhances absorption coefficient in solution. In addition, the TBFT-TR molecule exhibits a slightly greater tendency to form crystalline domains than the BDT-containing analogue, leading to slightly larger molecular ordering features and slightly higher hole transport property. Importantly, the annealed TBFT-TR:Y6 system shows the higher and more balanced charge carrier mobility, better charge pathway and suitable molecular ordering in the blend films compared to the BDTT-TR:Y6 system. These excellent features yield a superior PCE of 14.03% for the TBFT-TR-based devices, which is much higher than that of the BDTT-TR-based devices (12.18%). More importantly, devices based on other acceptors including $PC_{71}BM$, IDIC and Y6-C2 are further fabricated. Better device performance can also be obtained in the TBFT-TR-based devices. Overall, this work sheds light on the unique advantages of TBF-containing small molecule for preparing high performance OSCs, indicating a bright future for commercial applications.

Acknowledgements This work was supported by the National Natural Science Foundation of China (21702154, 51773157), the Fundamental Research Funds for the Central Universities and the Opening Project of Key Laboratory of Materials Processing and Mold and Beijing National Laboratory for Molecular Sciences (BNLMS201905).

Conflict of interest The authors declare that they have no conflict of interest.

Supporting information The supporting information is available online at http://chem.scichina.com and http://link.springer.com/journal/11426. The supporting materials are published as submitted, without typesetting or editing. The responsibility for scientific accuracy and content remains entirely with the authors.

1 Sun R, Wu Q, Guo J, Wang T, Wu Y, Qiu B, Luo Z, Yang W, Hu Z, Guo J, Shi M, Yang C, Huang F, Li Y, Min J. *Joule*, 2020, 4: 407–419
2 Zhou R, Jiang Z, Yang C, Yu J, Feng J, Adil MA, Deng D, Zou W, Zhang J, Lu K, Ma W, Gao F, Wei Z. *Nat Commun*, 2019, 10: 5393
3 Guo J, Bin H, Wang W, Chen B, Guo J, Sun R, Zhang ZG, Jiao X, Li Y, Min J. *J Mater Chem A*, 2018, 6: 15675–15683
4 Wang W, Sun R, Guo J, Guo J, Min J. *Angew Chem Int Ed*, 2019, 58: 14556–14561
5 Tang H, Xu T, Yan C, Gao J, Yin H, Lv J, Singh R, Kumar M, Duan T, Kan Z, Lu S, Li G. *Adv Sci*, 2019, 6: 1901613
6 Chen H, Hu D, Yang Q, Gao J, Fu J, Yang K, He H, Chen S, Kan Z, Duan T, Yang C, Ouyang J, Xiao Z, Sun K, Lu S. *Joule*, 2019, 3: 3034–3047
7 Wang Y, Wang Y, Kan B, Ke X, Wan X, Li C, Chen Y. *Adv Energy Mater*, 2018, 8: 1802021
8 Kwon OK, Park JH, Kim DW, Park SK, Park SY. *Adv Mater*, 2015, 27: 1951–1956
9 Cui Y, Yao H, Zhang J, Zhang T, Wang Y, Hong L, Xian K, Xu B, Zhang S, Peng J, Wei Z, Gao F, Hou J. *Nat Commun*, 2019, 10: 2515
10 Jiang K, Wei Q, Lai JYL, Peng Z, Kim HK, Yuan J, Ye L, Ade H, Zou Y, Yan H. *Joule*, 2019, 3: 3020–3033
11 Yuan J, Huang T, Cheng P, Zou Y, Zhang H, Yang JL, Chang SY, Zhang Z, Huang W, Wang R, Meng D, Gao F, Yang Y. *Nat Commun*, 2019, 10: 570
12 Fan Q, Su W, Wang Y, Guo B, Jiang Y, Guo X, Liu F, Russell TP, Zhang M, Li Y. *Sci China Chem*, 2018, 61: 531–537
13 Kan B, Feng H, Yao H, Chang M, Wan X, Li C, Hou J, Chen Y. *Sci China Chem*, 2018, 61: 1307–1313
14 Zhou Z, Liu W, Zhou G, Zhang M, Qian D, Zhang J, Chen S, Xu S, Yang C, Gao F, Zhu H, Liu F, Zhu X. *Adv Mater*, 2019, 32: 1906324
15 Xu X, Feng K, Bi Z, Ma W, Zhang G, Peng Q. *Adv Mater*, 2019, 31: 1901872
16 Fan B, Zhang D, Li M, Zhong W, Zeng Z, Ying L, Huang F, Cao Y. *Sci China Chem*, 2019, 62: 746–752
17 Qin J, An C, Zhang J, Ma K, Yang Y, Zhang T, Li S, Xian K, Cui Y, Tang Y, Ma W, Yao H, Zhang S, Xu B, He C, Hou J. *Sci China Mater*, 2020, https:doi.org/10.1007/s40843-020-1269-9
18 Ge J, Xie L, Peng R, Fanady B, Huang J, Song W, Yan T, Zhang W, Ge Z. *Angew Chem Int Ed*, 2020, 59: 2808–2815
19 Li ZY, Zhong WK, Ying L, Li N, Liu F, Huang F, Cao Y. *Chin J Polym Sci*, 2020, 38: 323–331
20 Zhang Z, Wang T, Ding Z, Miao J, Wang J, Dou C, Meng B, Liu J, Wang L. *Macromolecules*, 2019, 52: 8682–8689
21 Wadsworth A, Hamid Z, Bidwell M, Ashraf RS, Khan JI, Anjum DH, Cendra C, Yan J, Rezasoltani E, Guilbert AAY, Azzouzi M, Gasparini N, Bannock JH, Baran D, Wu H, de Mello JC, Brabec CJ, Salleo A, Nelson J, Laquai F, McCulloch I. *Adv Energy Mater*, 2018, 8: 1801001
22 Luponosov YN, Min J, Solodukhin AN, Bakirov AV, Dmitryakov PV, Shcherbina MA, Peregudova SM, Cherkaev GV, Chvalun SN, Brabec CJ, Ponomarenko SA. *J Mater Chem C*, 2016, 4: 7061–7076
23 Babics M, Liang RZ, Wang K, Cruciani F, Kan Z, Wohlfahrt M, Tang MC, Laquai F, Beaujuge PM. *Chem Mater*, 2018, 30: 789–798
24 Yue Q, Wu H, Zhou Z, Zhang M, Liu F, Zhu X. *Adv Mater*, 2019, 31: 1904283
25 Aarnio H, Sehati P, Braun S, Nyman M, de Jong MP, Fahlman M, Österbacka R. *Adv Energy Mater*, 2011, 1: 792–797
26 Huo Y, Gong XT, Lau TK, Xiao T, Yan C, Lu X, Lu G, Zhan X, Zhang HL. *Chem Mater*, 2018, 30: 8661–8668
27 Kim Y, Cook S, Tuladhar SM, Choulis SA, Nelson J, Durrant JR, Bradley DDC, Giles M, McCulloch I, Ha CS, Ree M. *Nat Mater*, 2006, 5: 197–203

28 Alqahtani O, Babics M, Gorenflot J, Savikhin V, Ferron T, Balawi AH, Paulke A, Kan Z, Pope M, Clulow AJ, Wolf J, Burn PL, Gentle IR, Neher D, Toney MF, Laquai F, Beaujuge PM, Collins BA. *Adv Energy Mater*, 2018, 8: 1702941
29 Wang Z, Zhu L, Shuai Z, Wei Z. *Macromol Rapid Commun*, 2017, 38: 1700470
30 Hoth CN, Choulis SA, Schilinsky P, Brabec CJ. *J Mater Chem*, 2009, 19: 5398
31 Collins SD, Ran NA, Heiber MC, Nguyen TQ. *Adv Energy Mater*, 2017, 7: 1602242
32 Bin H, Yang Y, Zhang ZG, Ye L, Ghasemi M, Chen S, Zhang Y, Zhang C, Sun C, Xue L, Yang C, Ade H, Li Y. *J Am Chem Soc*, 2017, 139: 5085–5094
33 Wang JL, Liu KK, Yan J, Wu Z, Liu F, Xiao F, Chang ZF, Wu HB, Cao Y, Russell TP. *J Am Chem Soc*, 2016, 138: 7687–7697
34 Yang L, Zhang S, He C, Zhang J, Yang Y, Zhu J, Cui Y, Zhao W, Zhang H, Zhang Y, Wei Z, Hou J. *Chem Mater*, 2018, 30: 2129–2134
35 Qiu L, Yuan J, He D, Zhang ZG, Li Y, Zou Y. *Dyes Pigments*, 2017, 140: 337–345
36 He D, Qiu L, Yuan J, Zhang ZG, Li Y, Zou Y. *Polymer*, 2017, 114: 348–354
37 Fan L, Cui R, Guo X, Qian D, Qiu B, Yuan J, Li Y, Huang W, Yang J, Liu W, Xu X, Li L, Zou Y. *J Mater Chem C*, 2014, 2: 5651
38 Dou K, Wang X, Du Z, Jiang H, Li F, Sun M, Yang R. *J Mater Chem A*, 2019, 7: 958–964
39 Min J, Cui C, Heumueller T, Fladischer S, Cheng X, Spiecker E, Li Y, Brabec CJ. *Adv Energy Mater*, 2016, 6: 1600515
40 Cui C, Guo X, Min J, Guo B, Cheng X, Zhang M, Brabec CJ, Li Y. *Adv Mater*, 2015, 27: 7469–7475
41 Yuan J, Zhang Y, Zhou L, Zhang G, Yip HL, Lau TK, Lu X, Zhu C, Peng H, Johnson PA, Leclerc M, Cao Y, Ulanski J, Li Y, Zou Y. *Joule*, 2019, 3: 1140–1151
42 Wei G, Wang S, Sun K, Thompson ME, Forrest SR. *Adv Energy Mater*, 2011, 1: 184–187
43 Gao W, Zhang M, Liu T, Ming R, An Q, Wu K, Xie D, Luo Z, Zhong C, Liu F, Zhang F, Yan H, Yang C. *Adv Mater*, 2018, 30: 1800052
44 Gao W, Liu T, Zhong C, Zhang G, Zhang Y, Ming R, Zhang L, Xin J, Wu K, Guo Y, Ma W, Yan H, Liu Y, Yang C. *ACS Energy Lett*, 2018, 3: 1760–1768
45 Li Z', Zhu Z, Chueh CC, Jo SB, Luo J, Jang SH, Jen AKY. *J Am Chem Soc*, 2016, 138: 11833–11839
46 Wang T, Sun R, Xu S, Guo J, Wang W, Guo J, Jiao X, Wang J, Jia S, Zhu X, Li Y, Min J. *J Mater Chem A*, 2019, 7: 14070–14078
47 Luo Z, Sun R, Zhong C, Liu T, Zhang G, Zou Y, Jiao X, Min J, Yang C. *Sci China Chem*, 2020, 63: 361–369
48 Min J, Luponosov YN, Gasparini N, Richter M, Bakirov AV, Shcherbina MA, Chvalun SN, Grodd L, Grigorian S, Ameri T, Ponomarenko SA, Brabec CJ. *Adv Energy Mater*, 2015, 5: 1500386